Cross-Calibration of HJ-1/CCD Over a Desert Site Using Landsat ETM+ Imagery and ASTER GDEM Product

Bo Zhong, Yuhuan Zhang, Tengteng Du, Aixia Yang, Wenbo Lv, and Qinhuo Liu

***Abstract*—The charge-coupled device (CCD) is visible to near-infrared imaging sensors onboard the Chinese Huan Jing 1 satellites. Like many sensors, the CCD lack onboard calibration capabilities, so alternative methods are required, e.g., cross-calibration. The wide field of view of the CCD sensors provides challenges for cross-calibration with narrow field of view sensors. We developed a technique to take advantage of a site with a uniform surface material and a natural topographic variation. Due to the topography, near-nadir Landsat Enhanced Thematic Mapper (TM) Plus (ETM+) observations actually see the material at a wide range of illumination and viewing angles. These observations and Advanced Spaceborne Thermal Emission and Reflection Radiometer global digital elevation model data were used to develop a model of this site's bidirectional reflectance distribution function that covered most of the illumination and view angle range of the CCD data. We validated this model by comparing the simulations to actual ETM+ and TM surface reflectances. The validated model was then used to calibrate the CCD instruments. The results were consistent to within 5% of field intensive vicarious calibration data.**

***Index Terms*—Bidirectional reflectance distribution function (BRDF), cross-calibrate, digital elevation model (DEM), Huan Jing 1 (HJ-1)/charge-coupled device (CCD), top-of-atmosphere (TOA) reflectance, vicarious calibration.**

I. Introduction

THE charge-coupled device (CCD) camera is one of the key instruments operating on the environment and disaster monitoring and forecasting satellite constellation, which is called as Huan Jing 1 in Chinese and abbreviated as HJ-1 (hereafter, the CCD camera onboard the HJ-1 satellite is written as HJ-1/CCD), launched on September 6, 2008, by the China Centre for Resources Satellite Data and Application (CRESDA). The HJ-1 satellite constellation is composed of three satellites, named as HJ-1A, HJ-1B, and HJ-1C, respectively. HJ-1A has two CCD cameras and one hyperspectral instrument onboard, and HJ-1B has two CCD cameras and one infrared camera onboard; HJ-1C is a synthetic aperture radar satellite, and it is launched on November 19, 2012. For CCD cameras, the nominal spatial resolution is 30 m. HJ-1/CDD has three visible bands (430–520, 520–600, and 630–690 nm) and one near-infrared (NIR) band (760–900 nm). HJ-1A and B have two CCD cameras onboard, respectively; therefore, four CCD cameras are working simultaneously in this satellite constellation, which makes a swath of about 700 km wide for each satellite and a revisit period of 48 h. The four CCDs are called HJ-1A/CCD1, HJ-1A/CCD2, HJ-1B/CCD1, and HJ-1B/CCD2, respectively. The primary characteristics are listed in Table I. The features of wide coverage, high spatial resolution, and high temporal observation frequency provide useful measurements for regional and global applications on agriculture, environment, and land survey. However, due to lack of onboard calibration system, vicarious calibration needs to be done every other time, and the frequency is usually once a year and will be increased with the aging of instruments. CRESDA performs the vicarious calibration measurements and releases the calibration coefficients once a year through its Web site at http://www.cresda.com. However, since the CCD cameras are not the state-of-the-art instruments, the radiometric capability is not so stable that it does not change for a whole year.

Since the launch of Landsat 1 in 1972, the imagery from Landsat series of satellites has become the longest continuous data set of high-spatial-resolution imagery for Earth observing, which are used widely for many kinds of remote sensing applications, such as land surface parameter retrieval, land use, and land-cover change [1]. It can be attributed to the knowledge of the radiometric properties of the Landsat sensors, which has been achieved through the combination of pre- and postlaunch efforts using laboratory, onboard, and vicarious calibration methods [1]. The calibration trends of Enhanced Thematic Mapper (TM) Plus (ETM+) and TM sensors are well described. Precise calibration of the ETM+ was given high priority during the development of the sensor [2]. The ETM+ has been described as the most stable of the Landsat sensors, changing no more than 0.5% per year in its radiometric

Manuscript received January 30, 2013; revised November 20, 2013, January 16, 2014, and February 14, 2014; accepted March 3, 2014. Date of publication March 27, 2014. This work was supported in part by the National High Technology Research and Development Program of China under Grant 2012AA12A304, by the Chinese Academy of Sciences Action Plan for West Development Project under Grant KZCX2-XB3-15, and by the National High Technology Research and Development Program of China under Grants 2013AA12A301 and 2009AA122002.

B. Zhong and Q. Liu are with the State Key Laboratory of Remote Sensing Science, Institute of Remote Sensing and Digital Earth, Chinese Academy of Science, Beijing 100101, China (e-mail: bzhong1@gmail.com, qhliuirsa.ac.cn).

Y. Zhang is with the State Environmental Protection Key Laboratory of Satellite Remote Sensing, Institute of Remote Sensing and Digital Earth, Chinese Academy of Sciences, Beijing 100101, China (e-mail: mermaid444@126.com).

T. Du is with Space Star Technology Company, Ltd., Beijing, 100086, China (e-mail: dutengteng1@163.com).

A. Yang is with the College of Computer Science and Technology Chongqing University of Posts and Telecommunications, Chongqing, 400065, China (e-mail: 815020350@qq.com).

W. Lv is with the College of Geosciences and Environmental Engneering, Southwest Jiaotong University, Chengdu, 611756, China (e-mail: wenber89@gmail.com).

Color versions of one or more of the figures in this paper are available online at http://ieeexplore.ieee.org.

Digital Object Identifier 10.1109/TGRS.2014.2310233

0196-2892 © 2014 IEEE. Personal use is permitted, but republication/redistribution requires IEEE permission.
See http://www.ieee.org/publications_standards/publications/rights/index.html for more information.

TABLE I
PRIMARY CHARACTERISTICS OF HJ-1/CCDS

Satellite	Sensor	Band	Spectral Range (nm)	Spatial Resolution (m)	Swath Width (km)	Revisit Period (hours)
HJ-1A/B	CCD1 and CCD2	1	430-520	30	360 for one camera; ~700 for one satellite (A/B)	96 hours for one satellite; 48 hours for A and B together
		2	520-600	30		
		3	630-690	30		
		4	700-900	30		

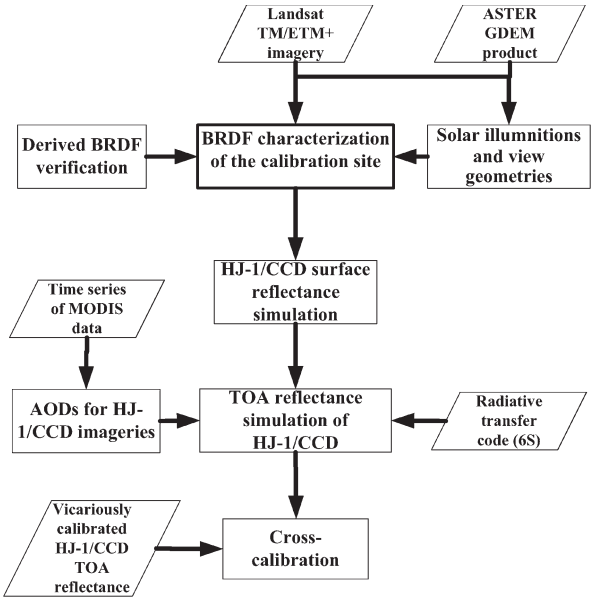

Fig. 1. Illustration of the procedure of the new cross-calibration approach. (Parallelogram is the input, and rectangle is the process.)

calibration, with an absolute calibration generally consistent to within 5% of other methods and sensors [4].

Early in the Landsat-7 mission, from June 1 to 4, 1999, the Landsat-5 and Landsat-7 satellites were placed in tandem orbit, and TM data were calibrated to the newer sensor to ensure calibration continuity between ETM+ and TM [5]. Since the original calibration scheme using the lamps for Landsat 5 no longer works effectively, changes to the radiometric calibration of the TM were implemented in May 2003 by the U.S. Geological Survey [6]. The new calibration procedure is based on a lifetime radiometric calibration curve derived from the sensor's internal calibrator, cross-calibration with the ETM+, and vicarious measurements [7], [8]. Vicarious studies carried out to date have suggested a relatively constant radiometric response for TM since 1988 [9].

In this paper, we present and validate a cross-sensor calibration technique for moderate- to high-spatial-resolution data with large-angle observation like HJ-1/CCD data. In this method, the well-calibrated nadir-view Landsat TM/ETM+ data and Advanced Spaceborne Thermal Emission and Reflection Radiometer (ASTER) global digital elevation model (DEM) (GDEM) product are first used together to fit the bidirectional reflectance distribution function (BRDF) characterization of a desert calibration site located in northern China. The retrieved BRDF is then used to simulate the surface reflectance under the solar illumination and view geometries of HJ-1/CCD. Third, the simulated surface reflectance of HJ-1/CCD is recalculated to the top-of-atmosphere (TOA) reflectance using the atmosphere radiative transfer model. At last, the cross-calibration of HJ-1/CCD is performed. The procedure is illustrated in Fig. 1, and the major steps are discussed in the following in detail.

II. METHODOLOGY

A. Calibration Site Choosing

In this paper, a portion of Badain Jaran Desert, which is an area of 1000 × 1000 pixels and about 30 × 30 km, located in central Inner Mongolia of northern China [see Fig. 2(a): broad view of the calibration site; the darkened area in the image is the location of the calibration site] is selected as the calibration site for three reasons as follows.

1) The site is temporally, spatially, and radiometrically stable, so it can be seen as an invariant object. The stability verification is carried out as follows.

   Desert areas are usually stable and homogeneous, and they appear to be very suitable for cross-calibration [9], [10]. Cosnefroy *et al.* [11] proposed a method for calibration site choosing, and a selection of candidate sites was given out, which is historically considered at the Centre National d'Etudes Spatiales (CNES) as a reference of calibration sites [12]. The important characteristics for calibration site choosing include brightness, spatial homogeneity, altimetry, bidirectional effects, seasonal variation, and long-term stability [12]. The characteristics of Badain Jaran desert are described as follows.

   a) *Brightness*. The mean surface reflectances of the calibration site are 0.0996, 0.1705, 0.2315, and 0.2699 in blue, green, red, and NIR bands, respectively, and the surface reflectance of different years is listed in Table III.

   b) *Spatial homogeneity*. It defines the radiometric uniformity over the calibration site. In this case, the TM/ETM+ imagery has 30-m spatial resolution, so different pixels show different slope properties, which determines the reflectance variation; however, the pixels with very similar slope properties (slope and aspect) are distributed randomly in the images, and the reflectance variation of these pixels is used to verify the radiometric uniformity over the calibration site. The mean reflectance and its standard deviation of the calibration site are listed in Table II. The deviations

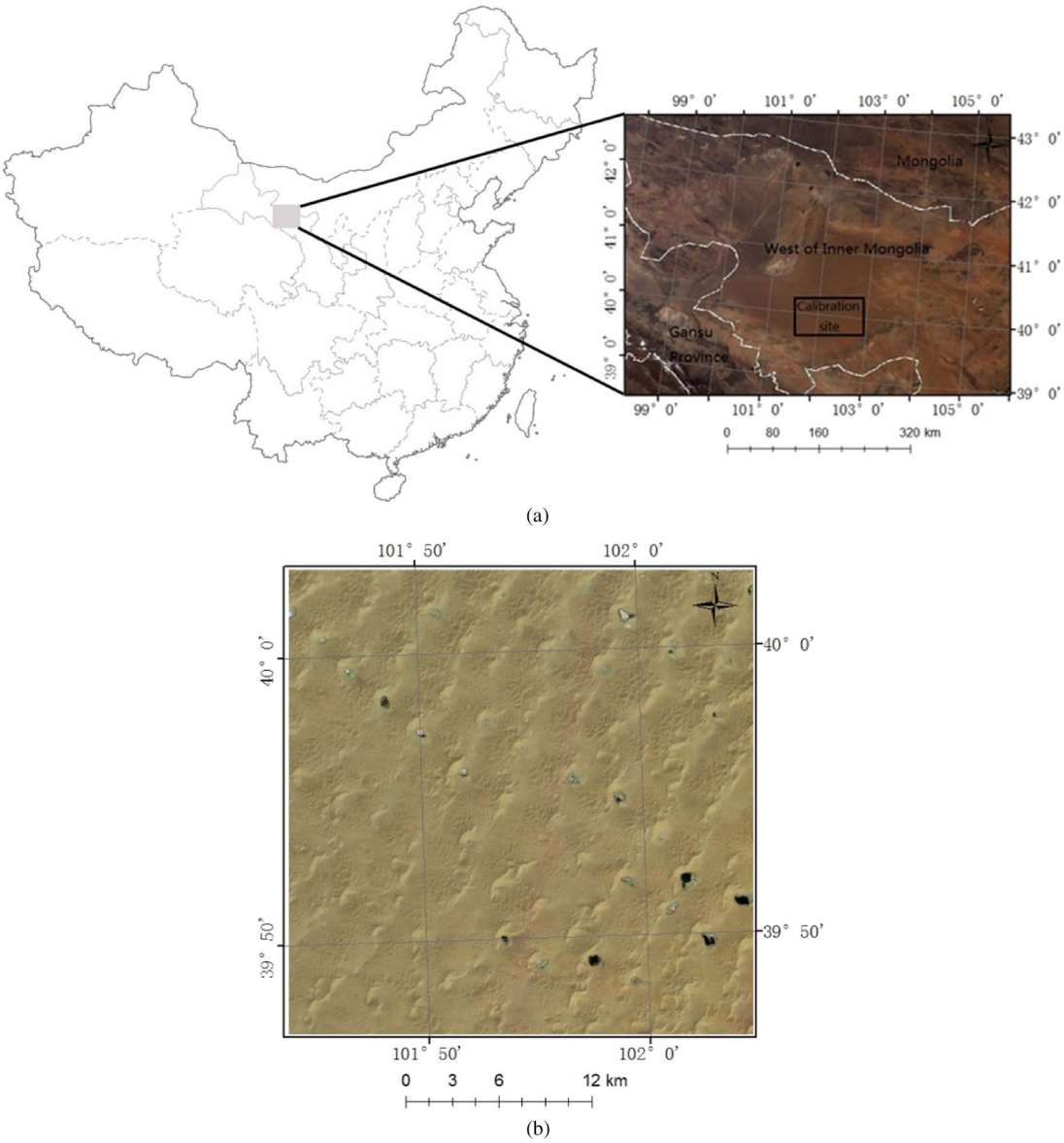

Fig. 2. Location and close view of the calibration site. (a) Location of the calibration site and a true color composite from MODIS imagery. (b) Close view of the site from a true color composite of Landsat ETM+ imagery.

TABLE II
MEAN REFLECTANCE AND ITS STANDARD DEVIATION OF THE CALIBRATION SITE WITH SIMILAR SLOPE PROPERTIES

band	Mean Slope (°)	Stdev of Slope (°)	Mean Aspect (°)	Stdev of Aspect (°)	Mean Reflectance	Stdev of Reflectance	Deviation (%)
1	25.584	0.303	195.613	0.385	0.101	0.002	1.87
2					0.165	0.005	3.23
3					0.252	0.016	6.17
4					0.307	0.020	6.47

for bands 1, 2, 3, and 4 are 1.87%, 3.23%, 6.17%, and 6.47%, respectively. Usually, the deviation is required to be less than 3% for 1-km spatial resolution data [11]; however, the optimal region for calibration may be located in the less homogeneous region as opposed to the more homogeneous region [12], such as Egypt-1 site [12], Libya-2, and Arabia-3 selected by CNES [13], which have deviations higher than 6%.

c) *Altimetry and bidirectional effects*. The altitude of the site is documented using ASTER GDEM data. This information is useful, because variation of the altitude inside the site may lead to variation of the bidirectional properties and the spatial homogeneity. The altitude and standard deviation are 1276.33 and 58.45 m, respectively. The BRDF or bidirectional effect describes how the site reflectance varies with viewing and solar

TABLE III
STATISTICS OF EVERY IMAGE FOR BAND 1

Image acquiring Date (YYYY.MM.DD)	Min reflectance	Max reflectance	Mean reflectance	Standard deviation	Linear fitting equation	R^2	Deviation in one image (%)	Deviation with time (%)
2000.03.03	0.074	0.130	0.098	0.013	——	——	13.3	1.3
2000.03.11	0.081	0.127	0.102	0.011	y=1.02*x+0.002	0.997	11.0	2.3
2001.02.10	0.071	0.143	0.101	0.017	y=1.11*x-0.002	0.993	17.1	1.7
2001.03.06	0.073	0.124	0.096	0.012	y=0.96*x+0.002	0.996	12.7	3.3
2002.03.26	0.072	0.121	0.102	0.010	y=1.02*x+0.003	0.988	10.2	2.2
2003.03.20	0.077	0.126	0.100	0.012	y=0.99*x+0.003	0.996	.11.6	0.4
2003.03.28	0.082	0.112	0.098	0.008	y=0.98*x+0.003	0.993	8.0	1.2
2004.02.12	0.066	0.137	0.098	0.017	y=1.00*x+0.001	0.986	17.2	1.4
2004.03.22	0.067	0.116	0.098	0.012	y=0.90*x+0.001	0.997	12.0	1.2
2010.02.03	0.073	0.139	0.101	0.016	y=1.11*x-0.003	0.995	.15.4	1.8
Mean			**0.100**	**0.013**		**0.993**	**12.8**	**1.7**

TABLE IV
STATISTICS OF AVERAGING ALL IMAGES BY SPECTRAL BAND

Band	Mean reflectance	Mean Standard deviation	Mean R^2	Mean deviation in the calibration site	Mean deviation in 10 years (%)
1	0.100	0.013	0.993	12.8	1.7
2	0.170	0.020	0.986	11.6	2.9
3	0.232	0.030	0.993	12.9	0.9
4	0.270	0.035	0.993	13.0	1.0

angles. For images with 30-m spatial resolution, the variation of the altitude leads to the variation of directional reflectance. Table III lists the mean surface reflectance and its standard deviation, which reflect the reflectance variations caused by bidirectional effects. The suggested reflectance variation is about 15%, and the values in the mean deviation column in Table IV reflecting the reflectance variation are about 12.8%, 11.6%, 12.9%, and 13.0% at bands 1, 2, 3, and 4, respectively, which are all less than 15%.

d) *Seasonal variation*. It is referred to seasonal variation on the observed reflectance. This effect can attribute to two cases: 1) a seasonal variation of the surface, e.g., occurrence of rains or snow, and 2) a bidirectional variation, because the geometrical solar configuration evolves with time, which is linked to the bidirectional effects above. A desert site is usually dry, so the seasonal variation induced by surface variation is negligible.

e) *Long-term stability*. Although a desert site is supposed to be stable with time, ten TM/ETM+ images within ten years are used to verify the long-term stability of the site. The acquiring dates of images are listed in Table III. The mean reflectance and the standard deviation for all images by spectral band are calculated and listed in Table IV. The mean deviations of reflectance in ten years are 1.7%, 2.9%, 0.9%, and 1.0% for bands 1, 2, 3, and 4, respectively, which are less than 4% documented in [11]. In addition, the scatterplots of the reflectance between the image on March 3, 2000, and any other image (see Fig. 3) have a very high R^2 value, which is more than 0.98 and even 0.99; therefore, the calibration site has high radiometric and spatial stability. Thus, the long-term stability of the calibration site is excellent.

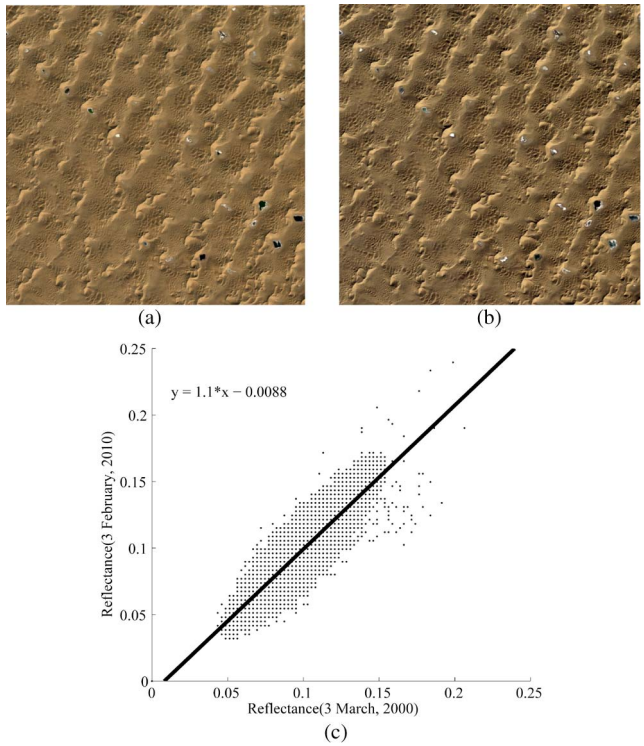

Fig. 3. Example for the stability verification of the calibration site. (a) Landsat imagery of calibration site on March 3, 2000. (b) Landsat imagery of calibration site on February 3, 2010. (c) Scatterplot of reflectance of the two images above.

2) There are a lot of lakes within the calibration site [see Fig. 2(b): true color composite of Landsat ETM+ image], which are seldom polluted, so the aerosol optical depth (AOD) of the calibration site can be determined accurately using the dark object (DO) method [14].
3) The surface material in the site is only sand, but the topography is hilly. This affords a wide range of local slopes and aspects of the same basic material, a natural data set for characterizing the material BRDF.

B. AOD Retrieval and Atmospheric Correction for Landsat TM and ETM+ Imagery

In order to accurately fit the site's BRDF characterization using Landsat TM/ETM+ imagery, the surface reflectance

TABLE V
EXAMPLE FOR THE 6S PARAMETER SETUP

Parameter	Value	Notation
Atmospheric model	Mid-latitude summer/winter	Depends on the date of image acquisition
Aerosol model	Shettle model for background desert aersol	For desert site
Solar zenith	Read from header file of the TM/ETM+ image	
Solar azimuth	Read from header file of the TM/ETM+ image	
View zenith	0	TM/ETM+ is nadir viewing
View azimuth	0	TM/ETM+ is nadir viewing
Wavelength	Blue band	
Surface reflectance	0	Clear water's reflectance is set as 0
AOD set	{0, 0.2, 0.5, 0.8, 1.0, 1.2, 1.5, 1.8, 2.0, 2.2, 2.5, 2.8, 3.0}	

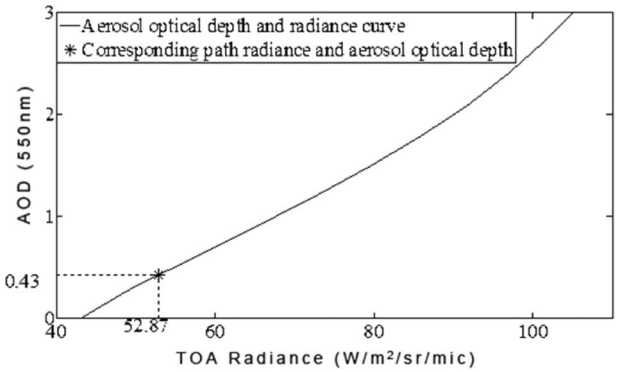

Fig. 4. Example for AOD retrieval using the DO method.

needs to be retrieved first. Since many clear lakes are within the calibration site, the DO method [14] is used to retrieve the AOD at 550 nm (hereafter, AOD is referred to AOD at 550 nm) for Landsat TM/ETM+ imagery. The DO method [14] is a widely used method for atmospheric correction of remotely sensed imagery nowadays, which has advantages of easy performing and high accuracy. This method supposes that there is an area in the image where the reflectance is so small that can be neglected (such as hill shading, dense vegetation, and clean water). The radiance of this area is then considered to be caused by atmosphere only, so the AOD can be calculated through radiative transfer code like 6S [15]. The clear lakes of the study area can be considered as DO to be used for atmospheric correction. Based on the DO method [14], we can set up the relationship between AOD and the TOA radiance for the study area. First of all, we need to set up a set of parameters for the 6S model as input, including atmospheric model, aerosol model, geometrical condition (including solar zenith, solar azimuth, view zenith, and view azimuth), wavelength, surface reflectance, and a set of AODs. For a given TM/ETM+ image, the parameters for the 6S model are set up like Table V. In the parameter table, only AOD can be changed, and every input AOD is corresponding to a TOA radiance as output. Consequently, the relationship between AOD and TOA radiance is set up. Fig. 4 shows an example of the relationship between AOD and TOA radiance. Therefore, the AOD for each image in this study can be estimated through the correlation like Fig. 4.

For example, for image on March 28, 2003, we can calculate its AOD as follows.

1) We get the image radiance based on its calibration coefficients.

TABLE VI
RETRIEVED AOD FOR LANDSAT TM AND ETM+ IMAGERY

ETM+ acquisition time (yyyy.mm.dd)	Retrieved AOD	TM acquisition time (yyyy.mm.dd)	Retrieved AOD
2000.03.03	0.15	2006.09.20	0.00
2000.04.29	0.00	2006.10.31	0.04
2001.10.16	0.022	2007.05.18	0.15
2001.11.17	0.00	2007.06.03	0.000
2002.01.04	0.07	2009.06.17	0.43
2002.03.18	0.28	2009.08.11	0.05
2002.05.28	0.33	2009.08.27	0.00
2002.09.17	0.11	2009.09.28	0.01
2002.11.04	0.36	2010.02.03	0.08
2002.11.13	0.03	2010.06.04	0.25
2002.12.15	0.125	2010.07.29	0.35
2003.03.28	0.43	2010.08.14	0.00
		2010.08.23	0.22

2) The radiance on the lake area of the blue band (52.87 w/m^2/sr/mic) is extracted from the image.
3) Based on the relationship between AOD and TOA radiance, the AOD is interpolated.

Based on the aforementioned method, we calculate the AODs for all 25 images in this study through 2000 to 2010, and the result is shown in Table VI.

Since the calibration site within an area of 30 km by 30 km is hardly influenced by human activities, the derived AODs for lake areas are used to correct the atmospheric effect for the whole calibration site.

C. Site's BRDF Fitting

As shown in Fig. 2(b), there are many different sizes of sand dunes within the site, so the topography of the site is hilly. Therefore, for every pixel in the image, the solar illuminations and view geometries corresponding to slopes are varying in a very large range. That is, the solar angles of slope (zenith and azimuth angles) and viewing angles of slope (zenith and azimuth angles) are varied pixel by pixel, although these pixels are all nadir viewed in Landsat TM/ETM+ imagery. Fig. 5

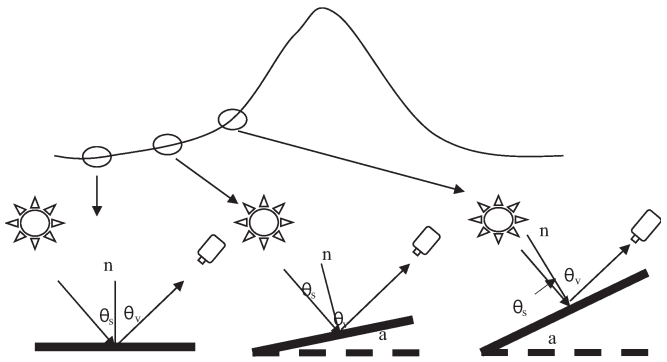

Fig. 5. Illustration of the solar illuminations and view geometries varying with slope in the calibration site. For different slope elements corresponding to different pixels in remotely sensed imagery, the solar illuminations and view geometries of slope are varying.

shows an example. For different slope elements corresponding to different pixels in remotely sensed imagery, the land surface is not changed, but the solar zenith of slope (θs) and view zenith of slope (θv) are so different. For this calibration site, only if the solar illuminations and view geometries of every pixel corresponding to slopes in nadir-viewing Landsat TM/ETM+ imagery are known, the BRDF can consequently be reconstructed.

1) Slope and Aspect Calculation: In order to get the solar illuminations and view geometries of slopes for every pixel in Landsat TM/ETM+ imagery, the ASTER GDEM product is used. The GDEM was created by stereo-correlating the 1.3 million scene ASTER visible/NIR archive, covering the Earth's land surface between 83° N and 83° S latitudes. The GDEM is produced with 30-m postings and is formatted in 1×1 degree tiles as GeoTIFF files. Each GDEM file is accompanied by a Quality Assessment file, either giving the number of ASTER scenes used to calculate a pixel's value or indicating the source of external DEM data used to fill the ASTER voids.

Therefore, we use topographic modeling [16] on the ASTER GDEM product to extract parametric information, including slope and aspect, which can be calculated using

$$s = \arctan\sqrt{\left(\frac{\partial z}{\partial x}\right)^2 + \left(\frac{\partial z}{\partial y}\right)^2} \tag{1}$$

$$a = \cos^{-1}\left\{\frac{\frac{\partial z}{\partial y}}{\sqrt{\left(\frac{\partial z}{\partial x}\right)^2 + \left(\frac{\partial z}{\partial y}\right)^2}}\right\}, \quad \text{when } \frac{\partial z}{\partial x} \geq 0$$

$$a = \pi + \cos^{-1}\left\{\frac{\frac{\partial z}{\partial y}}{\sqrt{\left(\frac{\partial z}{\partial x}\right)^2 + \left(\frac{\partial z}{\partial y}\right)^2}}\right\}, \quad \text{when } \frac{\partial z}{\partial x} < 0 \tag{2}$$

where s is the slope and a is the aspect. The slope is measured in degrees with the convention of 0° for a horizontal plane and the aspect angle with the convention of 0° to the north (up) and angles increasing clockwise.

2) Solar Illuminations and View Geometry Calculation: For every pixel in a remotely sensed imagery, since the positions of sun and sensor are known, the solar illuminations and view geometries of slopes are determined by the slope and aspect

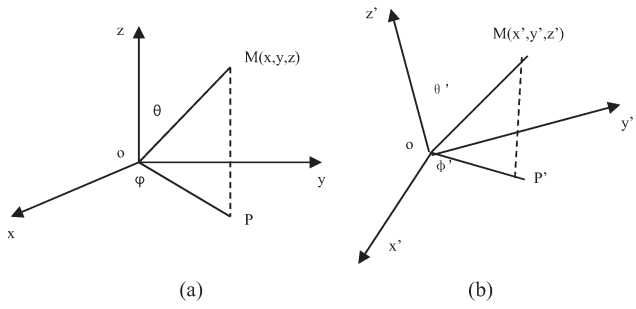

Fig. 6. Coordinate system and rotation. (a) Global coordinate system. (b) Local coordinate system.

only, which is depicted in Fig. 5. Since the slope and aspect can be calculated from the ASTER GDEM product, the pixel's solar illuminations and view geometries can be calculated. The method for calculating the solar illuminations and view geometries is as follows.

After the slope and aspect for each pixel are calculated, a local coordinate system is built for each pixel [Fig. 6(b)].

The sun and view angles provided in Landsat TM/ETM+ data are in the global coordinate system [the xoy plane is built on the horizontal plane; see Fig. 6(a)]; consequently, the sun and view angles are the same for all pixels. The view zenith and azimuth angles are 0° in the global coordinate system because nadir-viewing Landsat TM/ETM+ imagery has a narrow swath. In order to get the incidence and view angles of every pixel in the local coordinate system, we need to convert the coordinates in the global coordinate system to those in the local coordinate system. The sun-view geometries of local systems are the real sun-view geometries of every pixel [Fig. 6(b)].

In Fig. 6, the M represents the sun position; the x-, y-, and z-axes represent the south, east, and zenith directions, respectively; θ is the solar zenith angle; and φ is the solar azimuth angle in the global coordinate system.

The transformation between the Descartes coordinate in the local coordinate system (x', y', z') and the Descartes coordinate in the global coordinate system (x, y, z) is described as

$$\begin{bmatrix} x' \\ y' \\ z' \end{bmatrix} = R_2 R_1 \begin{bmatrix} x \\ y \\ z \end{bmatrix} \tag{3}$$

$$R_1 = \begin{bmatrix} \cos\varphi_1 & \sin\varphi_1 & 0 \\ -\sin\varphi_1 & \cos\varphi_1 & 0 \\ 0 & 0 & 1 \end{bmatrix} \tag{4}$$

$$R_2 = \begin{bmatrix} \cos\theta_1 & 0 & \sin\theta_1 \\ 0 & 1 & 0 \\ \sin\theta_1 & 0 & \cos\theta_1 \end{bmatrix} \tag{5}$$

where φ_1 and θ_1 are the rotation angles corresponding to slope and aspect angles, respectively.

The solar zenith of slope can be also calculated quickly using the formula as follows [17]:

$$\cos\theta' = \cos\theta\cos s + \sin\theta\sin s\cos(\varphi - a) \tag{6}$$

where θ' is the solar zenith of slope, θ is the solar zenith of plane, φ is the solar azimuth of plane, s is the slope angle, and a is the aspect angle.

TABLE VII
STATISTICS OF VARIATION RANGE OF VIEW ZENITH OF SLOPE, SOLAR ZENITH OF SLOPE, AND RELATIVE AZIMUTH OF SLOPE OF LANDSAT ETM+ IMAGERY IN THE CALIBRATION SITE

Acquisition Time (yyyy.mm.dd)	Solar Elevation (°)	Solar Azimuth (°)	View Zenith Range of slope (°)	Solar Zenith Range of slope (°)	Relative Azimuth Range of slope (°)
2000.04.29	58.24	138.22	0~59.29	0.20-78.44	0.01-179.97
2002.03.18	42.85	145.10	0-59.29	0-89.97	0-180.00
2002.11.13	29.14	159.20	0-59.29	0-90.00	0-180.00
2002.12.15	23.30	158.37	0-59.29	0-90.00	0-179.99
2000.03.03	37.70	148.26	0-59.29	0-90.00	0-180.00
2002.05.28	63.35	128.57	0-59.29	0.13-71.95	0-179.95
2001.10.16	37.65	155.64	0-59.29	0-90.00	0.01-180.00
2001.11.17	28.08	159.50	0-59.29	0-90.00	0-180.00
2002.01.04	31.66	158.48	0-59.29	0-89.99	0-180.00
2002.09.17	47.22	147.01	0-59.29	0-89.19	0.04-179.99
2002.11.04	31.66	158.48	0-59.29	0-90.00	0-180.00
2003.03.28	46.62	143.55	0-59.29	0-89.10	0.01-179.99

The solar elevation (of plane), solar azimuth (of plane), solar zenith (θ'_s) range of slope, view zenith (θ'_v) range of slope, and relative azimuth (φ') range of slope for 12 scenes of Landsat ETM+ images are calculated and listed in Table VII.

3) Site's BRDF Characterization: From the statistics in Table VII, it is found that the view zenith ranges of slope from 0° to 59.29°, the solar zenith ranges of slope from 0° to almost 90°, and the relative azimuth ranges of slope from 0° to 180° for any Landsat ETM+ imagery; therefore, the variation range of solar illuminations and view geometries in just one scene of Landsat ETM+ imagery can be satisfied to fit the site's BRDF characterization. However, the solar zenith angles of slope for a specific solar illumination corresponding to a single ETM+ image mainly distribute within a specific range [see Fig. 7(a)]. For different solar illuminations, the ranges of solar zenith angle of slope are different [see Fig. 7(a)]; therefore, the solar zenith angles of slope will be evenly distributed within $0°-90°$ as long as there are enough solar illuminations corresponding to ETM+ images with different acquisition dates [see Fig. 7(b)]. Fig. 7(a) shows the distribution of solar zenith angle of slope for three different ETM+ images, and Fig. 7(b) shows the solar zenith angle of slope distribution for the combination of the three ETM+ images, which clearly shows that the solar zenith angle range of slope from three combined ETM+ images is more evenly distributed within 0°–90° than the solar zenith angle range of slope from any single ETM+ image.

Based on the aforementioned analysis, we use six scenes of Landsat ETM+ Level-1G data on different dates to better fit the BRDF of the calibration site. In this paper, in order to keep more information, we use 4-D surface (θ'_s, θ'_v, φ', and ρ; θ'_s, θ'_v, and φ' are the variables, and ρ is a value of surface reflectance) to characterize the site's BRDF instead of statistical BRDF models. The statistics of surface reflectance (ρ), solar zenith angle of slope (θ'_s), viewing zenith angle of slope (θ'_v), and

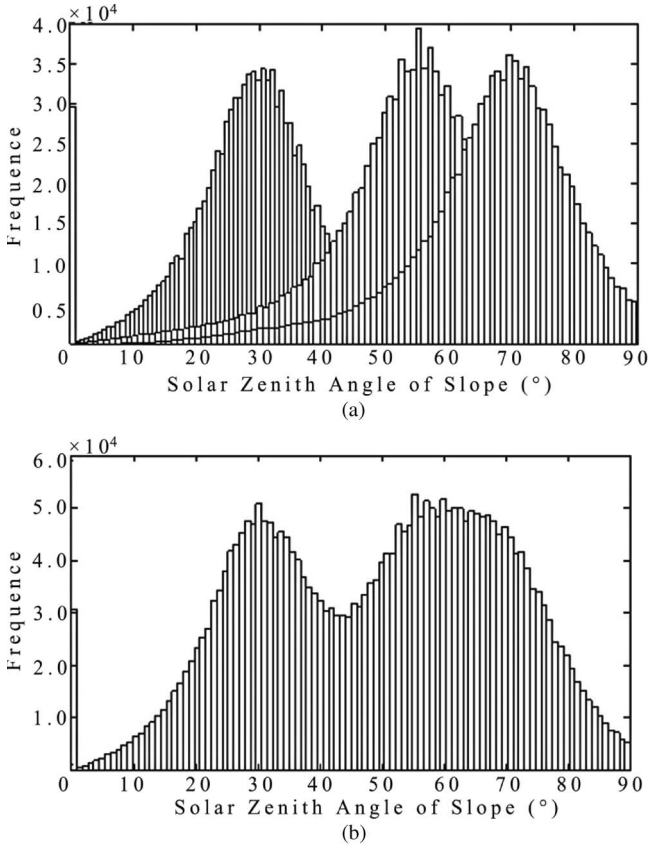

Fig. 7. Solar zenith angle of slope histogram of the calibration site. (a) Solar zenith angle of slope distribution range from single Landsat ETM+ image (images from left to right are May 28, 2002, March 3, 2000, and January 1, 2001, respectively). (b) Solar zenith angle of slope distribution from the combination of three Landsat ETM+ images.

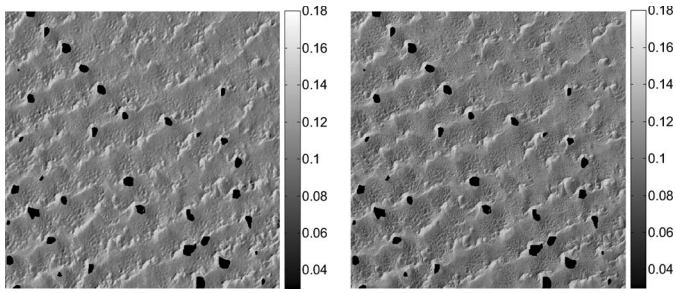

Fig. 8. Comparison between (left) the simulated Landsat ETM+ imagery and (right) the actual Landsat ETM+ imagery on October 16, 2001. The simulated image looks very similar to the actual image except that the spatial resolution of the simulated image looks coarser.

relative azimuth of slope (φ') are made from the six images. We then set up a mapping between the angles (variables) and the surface reflectance (function). In other words, the mapping is equivalent to a lookup table. The solar zenith angle of slope, observation zenith angle of slope, and relative azimuth angle of slope ($\theta'_s, \theta'_v, \varphi'$) are inputs, and the output is the surface reflectance (ρ). Therefore, for any combination of ($\theta'_s, \theta'_v, \varphi'$), the corresponding ρ can be obtained from the lookup table by interpolating. In practical use, the same combinations of ($\theta'_s, \theta'_v, \varphi'$) usually correspond to the different reflectance. However, under the circumstance, the mode value of ρ is used. The cubic interpolation function of Matlab (griddata3 function) is used in the simulation. The griddata3 function in Matlab first finds the

TABLE VIII
COMPARISON BETWEEN ACTUAL SURFACE REFLECTANCE AND THE SIMULATED ONE ON BAND 1

Acquisition time (yyyy.mm.dd)	Actual surface reflectance (ρ)	Simulated surface reflectance (ρ)'	Difference (ρ-ρ')	Difference error (%)
2006.09.20	0.0959	0.1030	-0.0071	7.4035
2006.10.31	0.1049	0.1073	-0.0024	2.2879
2007.05.18	0.0912	0.0932	-0.0020	2.1930
2007.06.03	0.0920	0.0935	-0.0015	1.6304
2009.06.17	0.0938	0.0934	0.0004	0.4264
2009.08.11	0.0941	0.0925	0.0016	1.7003
2009.08.27	0.0970	0.1044	-0.0074	7.6289
2009.09.28	0.0982	0.1024	-0.0042	4.2770
2010.02.03	0.0975	0.1057	-0.0082	8.4103
2010.06.04	0.0974	0.0935	0.0039	4.0041
2010.07.29	0.0919	0.0929	-0.0010	1.0881
2010.08.14	0.0946	0.0925	0.0021	2.2199
2010.08.23	0.1027	0.1044	-0.0017	1.6553

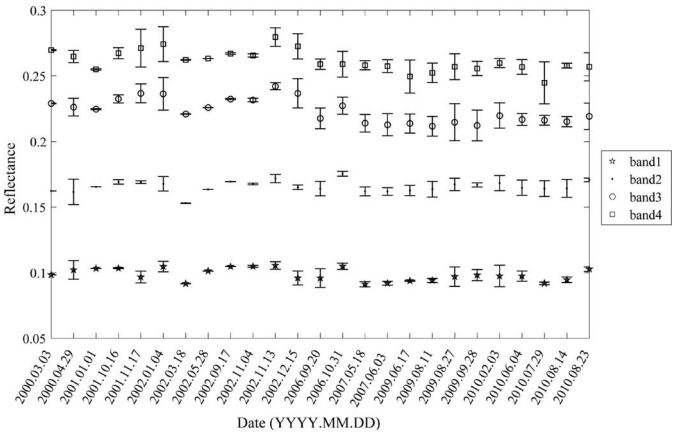

Fig. 9. Difference error between the actual surface reflectance and the simulated one for Landsat TM/ETM+ bands 1, 2, 3, and 4 corresponding to the lines in the figure from bottom to top, respectively.

discrete points according to the three features around the insert point by the Delaunay method. A triangle was then created by the three discrete points. Finally, the linear interpolation or the cubic equation interpolation could be chosen to calculate the value of any insert point within the triangle.

In order to verify the accuracy of the BRDF characterization, we use the 4-D surface to simulate the surface reflectance for all collected Landsat TM and ETM+ images. Fig. 8 shows an example of simulation for the Landsat ETM+ imagery on October 16, 2001. The mean surface reflectance of every image is then compared with that of the actual Landsat TM/ETM+ imagery (atmosphere corrected using the derived AOD in Table VI), and the comparison results for band 1 are listed in Table VIII. The difference errors in percentage for bands 1, 2, 3, and 4 are plotted in Fig. 9.

Comparing with the actual Landsat TM/ETM+ images, the mean difference errors of the simulated images are 2.68%, 1.92%, 2.68%, and 2.32% for bands 1, 2, 3, and 4, respectively. It is obvious that the derived BRDF characterization has very good agreement with the real situation. Therefore, the derived BRDF characterization can be used to simulate the surface reflectance of HJ-1/CCD effectively.

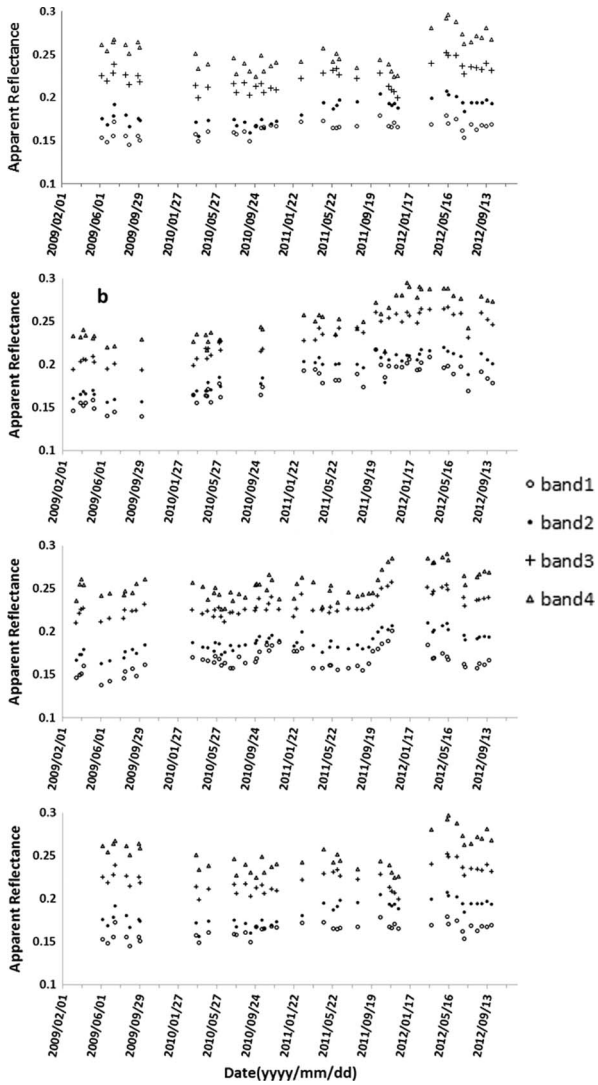

Fig. 10. Time series of TOA reflectance of HJ-1/CCDs from 2008 to 2012. (a) HJ-1A/CCD1. (b) HJ-1A/CCD2. (c) HJ-1B/CCD1. (d) HJ-1B/CCD2.

D. HJ-1/CCD Radiometric Characteristics

In order to have overall knowledge of the radiometric characteristics of HJ-1/CCDs, we plot out the four years' time

TABLE IX
INFORMATION OF THE SELECTED IMAGE PAIRS OF HJ-1B/CCD2 AND MODIS SATISFYING THE CRITERIA

Data	Acquiring date (YYYY/MM/DD)	Day of year	GMT time (H:MM)	Solar Elevation (°)	View zenith (°)
HJ1B-CCD2	2009/09/27	270	4:06	43.613	15.264
MODIS	2009/09/27	270	4:15		14.0644
HJ1B-CCD2	2010/08/24	236	3:59	57.656	22.7018
MODIS	2010/08/24	236	4:00		19.6168
HJ1B-CCD2	2011/11/15	319	3:50	26.593	16.8497
MODIS	2011/11/15	319	3:55		21.425
HJ1B-CCD2	2012/06/15	167	3:40	63.246	16.3272
MODIS	2012/06/15	167	4:15		11.8634

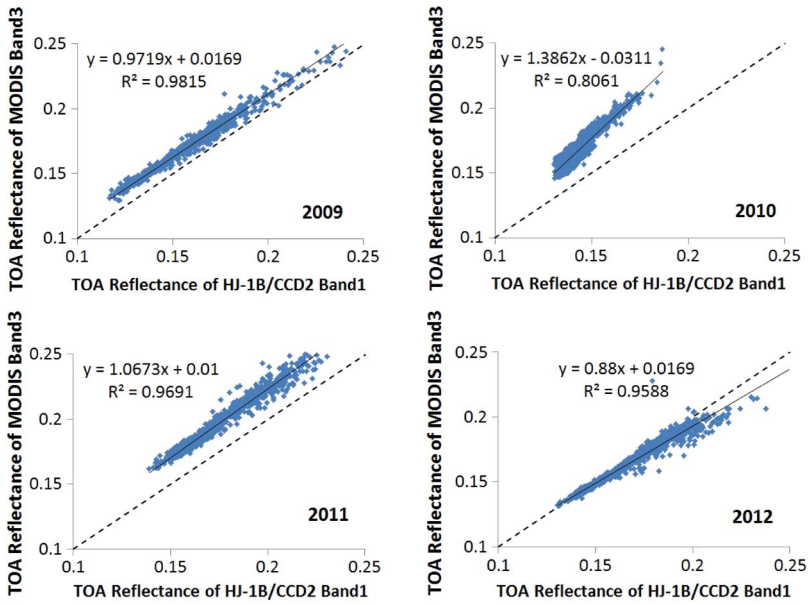

Fig. 11. Comparison of TOA reflectance between MODIS data and HJ-1B/CCD2 data with very high similarity on passing date–time and view geometry in (upper left) 2009, (upper right) 2010, (lower left) 2011, and (lower right) 2012. The dashed line is the 1 : 1 line, and the solid line is the linear fitting.

series of average TOA reflectance at the calibration site for each CCD in Fig. 10 using the calibration coefficients given by CRESDA. Although the calibration site is very stable with time, the average TOA reflectance of all four CCDs is varied year by year. From Fig. 10, the TOA reflectance variation between two years can reach 0.085, 0.065, 0.075, and 0.075 at blue, green, red, and NIR bands, respectively, which is close to 1/2 TOA reflectance on blue band and 1/3 TOA reflectance on NIR band. Furthermore, the variations do not just exist within a year but interyear, which is an obvious evidence showing that the calibration is not consistent year by year. In addition, all HJ-1/CCD data are manually checked to make sure that they are very clear (out of cloud and haze contamination), which minimizes the effects induced by atmosphere condition change. Some of the variations are maybe induced by the change of surface condition. In order to decouple the site changes with those experienced by the instrument, we use data from Moderate Resolution Imaging Spectroradiometer (MODIS) onboard the Terra satellite as reference to check the yearly variations of HJ-1/CCD data. MODIS is a state-of-the-art instrument with very high radiometric capacity and has very high temporal frequency, so we compare the apparent reflectance of HJ-1/CCD data with MODIS level-1b data (500-m resolution), including MOD02 (Level-1B Calibrated Geolocation Data Set) and MOD03 (Geolocation Data Set). In this comparison, the MODIS level-1b data from collection 6 are used because of their improved calibration [18] from collection 5. In order to make them comparable, we define several criteria: 1) They have very close passing time, which make them out of the influence of atmosphere condition change; 2) they have very close view zenith, getting rid of the bidirectional effect; 3) they are out of cloud contamination; and 4) the HJ-1/CCD is resampled to 500 m. The selected image pairs of HJ-1B/CCD2 and MODIS satisfying the aforementioned criteria and their information are listed in Table IX. We plot out the scatterplot of the apparent reflectance of the image pairs in Table IX. Fig. 11 gives an example of the scatterplot of blue band (band 3 of MODIS and band 1 of HJ-1/CCD) in 2009, 2010, 2011, and 2012. If we suppose that the radiometric stability of MODIS is good, the radiometry of HJ-1B/CCD2 is varied. The tendency of variation from Fig. 11 is the same as that from Fig. 10, which is that the TOA reflectance of the two data is consistent in 2009, the TOA reflectance of HJ-1B/CCD2 is lower in 2010 and 2011, and the TOA reflectance of HJ-1B/CCD2 is higher in 2012. Since the factors, including aerosol, cloud, weather, solar illumination, view geometry, and spatial resolution, are all considered and minimized, the calibration is the only reason for explaining the radiometric difference between MODIS and HJ-1/CCD data. We have done this work for all HJ-1/CCD data, and the slope, intercept, and R^2 are listed in Table X. Therefore, the yearly

TABLE X
SLOPE, INTERCEPT, AND R^2 OF THE SCATTERPLOT BETWEEN HJ-1/CCD AND MODIS IMAGE PAIRS WITH CLOSE PASSING DATE–TIME AND VIEW GEOMETRY

Sensor	Band	2009			2010			2011			2012		
		Slope	Intercept	R^2	Slope	Intercept	R^2	Slope	Intercept	R^2	Slope	Intercept	R^2
HJ-1A/CCD1	1	1.13	0.00	0.93	--	--	--	1.17	-0.02	0.97	1.00	0.02	0.94
	2	1.16	-0.01	0.91	--	--	--	1.24	-0.04	0.93	1.10	-0.00	0.91
	3	1.07	-0.01	0.90	--	--	--	1.15	-0.07	0.90	1.10	-0.02	0.90
	4	1.10	-0.02	0.88	--	--	--	1.32	-0.11	0.95	1.04	0.00	0.86
HJ-1A/CCD2	1	1.13	0.01	0.97	0.90	0.01	0.98	1.27	-0.05	0.76	0.70	0.03	0.73
	2	1.26	0.00	0.97	1.00	0.00	0.97	1.12	-0.02	0.77	0.70	0.04	0.64
	3	1.16	-0.00	0.97	0.88	0.02	0.96	0.88	0.03	0.54	0.63	0.06	0.51
	4	1.33	-0.04	0.96	1.09	0.02	0.96	0.93	0.04	0.52	0.71	0.06	0.52
HJ-1B/CCD1	1	1.22	0.02	0.84	1.00	0.01	0.97	1.08	0.00	0.98	1.25	-0.02	0.97
	2	1.28	-0.02	0.82	1.14	-0.02	0.90	1.10	-0.01	0.96	1.20	-0.04	0.96
	3	1.09	-0.01	0.82	1.00	-0.01	0.90	1.04	-0.01	0.96	1.16	-0.06	0.96
	4	1.07	-0.00	0.76	1.07	-0.01	0.91	1.14	-0.02	0.94	1.27	-0.09	0.95
HJ-1B/CCD2	1	0.97	0.02	0.98	1.39	-0.03	0.81	1.07	0.01	0.97	0.88	0.02	0.96
	2	1.00	0.01	0.97	1.26	-0.00	0.89	1.15	-0.03	0.96	0.91	0.00	0.94
	3	0.85	0.02	0.94	1.10	-0.07	0.89	0.99	-0.00	0.96	0.76	0.03	0.92
	4	0.84	0.03	0.95	1.13	0.00	0.86	1.09	-0.01	0.96	0.76	0.03	0.94

and interyear variations are mainly induced by radiometric calibration inconsistency. Thus, the cross-calibration of HJ-1/CCD is necessary.

E. HJ-1/CCD Cross-Calibration

In this paper, 36 scenes of HJ-1/CCD, including HJ-1A/CCD1, HJ-1A/CCD2, HJ-1B/CCD1, and HJ-1B/CCD2, from May to October, 2009 are chosen. All HJ-1/CCD images are listed in Table IV. The major steps of cross-calibration include the following: 1) HJ-1/CCD surface reflectance simulation; 2) AOD retrieval for HJ-1/CCD images; 3) HJ-1/CCD TOA reflectance simulation using the derived AOD and simulated surface reflectance from steps 1) and 2); and 4) comparison between simulated and actual HJ-1/CCD TOA reflectances.

1) HJ-1/CCD Surface Reflectance Simulation: First, the chosen HJ-1/CCD and ASTER GDEM product are used together to calculate the solar illuminations and view geometries for all HJ-1/CCD imageries.

Second, the calculated solar illuminations and view geometries are put into the derived BRDF characterization of the calibration site to simulate the surface reflectance for every HJ-1/CCD image.

Third, since the spectral responses of Landsat ETM+ and HJ-1/CCD are different, the spectral matching between the two different sensors needs to be done. Fig. 12 shows the spectral response profiles of HJ-1/CCDs and Landsat ETM+. The spectral matching factors are calculated to account for the difference induced by spectral response function between Landsat ETM+ and HJ-1/CCD. The spectral matching factor is defined as

$$a = \int_{\lambda_1}^{\lambda_2} \rho_\lambda * f_{\mathrm{HJ}}(\lambda) d\lambda \Big/ \int_{\lambda_3}^{\lambda_4} \rho_\lambda * f_{\mathrm{ETM}}(\lambda) d\lambda \qquad (7)$$

where a is the spectral matching factor; λ is the spectral wavelength; ρ_λ is the ground measured spectrum of the desert at the calibration site, which is plotted in Fig. 13; and $f_{\mathrm{HJ}}(\lambda)$ and $f_{\mathrm{ETM}}(\lambda)$ are the spectral response functions for HJ-1/CCD and Landsat ETM+ respectively. $\lambda_1 \sim \lambda_2$ is the spectral range of HJ-1/CCD; $\lambda_3 \sim \lambda_4$ is the spectral range of Landsat ETM+.

A guide from local travel agency drove us, a group of five persons, into the Badain Jaran desert on July 13–14, 2012. Along the driving route, 138 surface spectra of desert surface were measured using an SVC HR-1024 high-resolution field portable spectroradiometer on 20 spots, whose geographical coordinates are listed in Table XI. The detailed information of the spectroradiometer can be found at http://www.spectravista.com. The data were processed using the software provided with SVC HR-1024. Since the spectra of desert surface are very similar, we randomly take out 30 spectra from the 138 spectra to get an averaged spectrum, which is shown in Fig. 13. The averaged spectrum is used to calculate the spectral matching factor.

Based on the definition of spectral matching factor, the spectral matching factors of HJ-1/CCD to Landsat ETM+ are calculated and listed in Table XII.

2) AOD Retrieval: Since the calibration site is not only homogeneous but also covers an area of 30 km by 30 km only, we assume that the AOD variation is negligible. Therefore, we introduce an AOD retrieval algorithm by Liang and Zhong [19], [20], which takes full advantage of MODIS multitemporal observation capability. The central idea of this algorithm is to detect the "clearest" observation during a temporal window for each pixel. Therefore, only if the AODs for the "clearest" observations are known, the AODs of other "hazy" observations can be interpolated from the surface reflectance of the "clearest" observations [20].

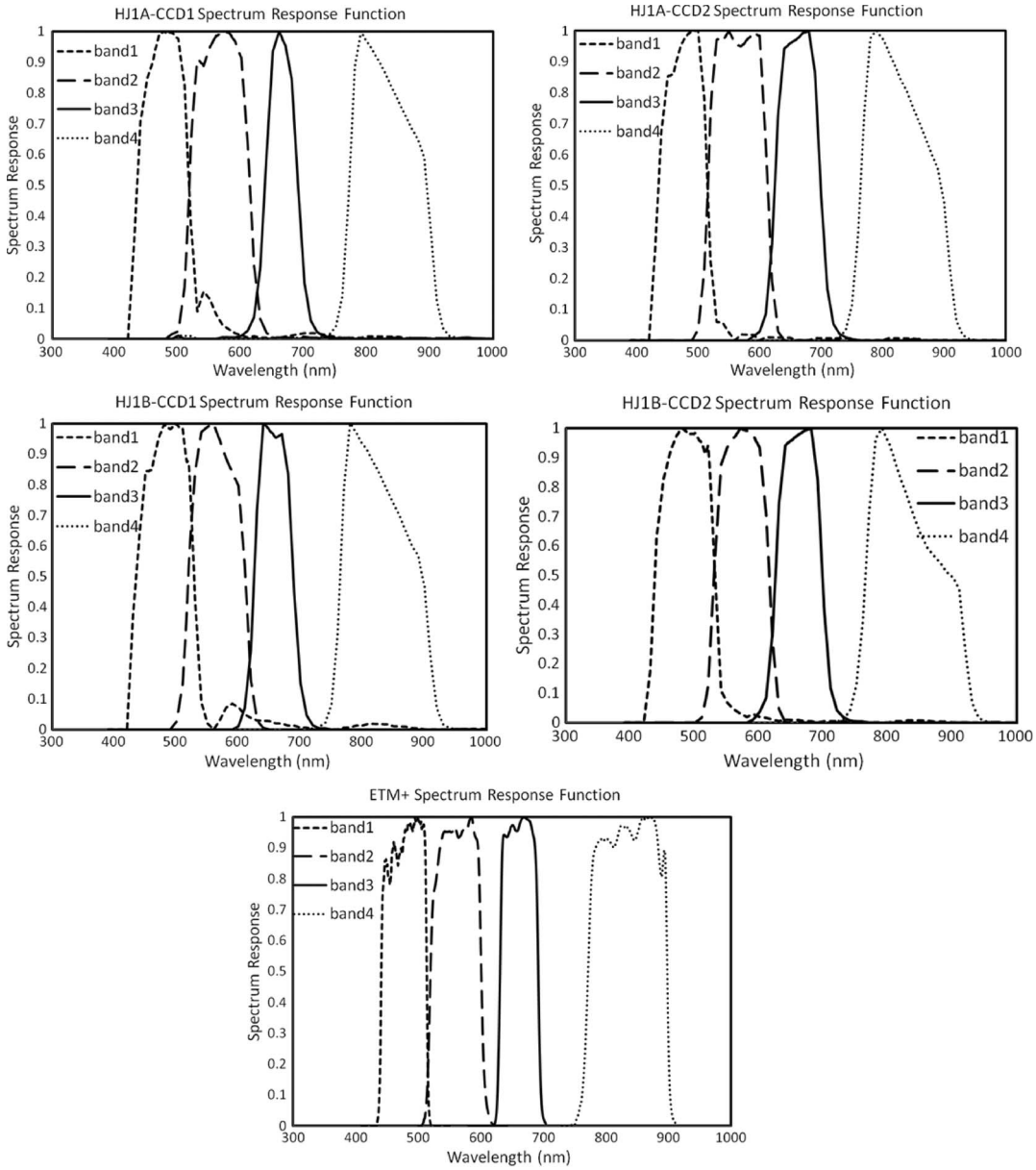

Fig. 12. Spectral response profiles of Landsat ETM+ and HJ-1A/CCDs in corresponding first to fourth wavelength regions.

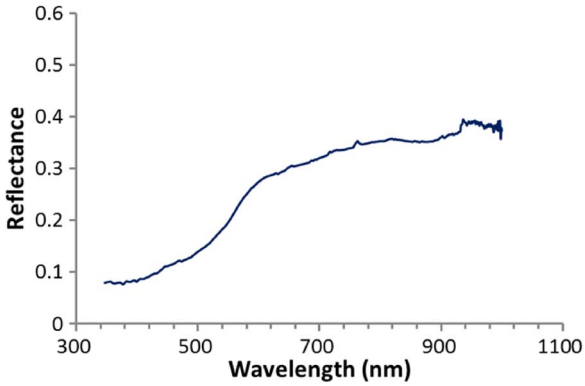

Fig. 13. Spectra plot of the desert at the calibration site.

For our study, we make four modifications for this algorithm to get more accurate site BRDF and AODs.

1) AOD determination for the "clearest" days: Since a lot of unpolluted lakes are located within the calibration site, the lowest AOD or the AOD for the "clearest" days can be determined by the DO method accurately using high-spatial-resolution remotely sensed imagery like Landsat TM and ETM+. The calculated AODs are listed in Table VI.
2) We shrink the use of the algorithm from global to the desert calibration site, which is stable, so it can take full advantage of this algorithm to get more accurate surface reflectance.
3) In the former algorithm [19], Liang *et al.* identify the "clearest" days using the minimum blue band TOA reflectance without considering the variation induced by view geometries; here, we identify the "clearest" observations for every 10° in view zenith angles from 0° to 50° (0–10, 11–20, 21–30, 31–40, and 41–50). Practically, when the view zenith angle is larger than 50°, the observation is pretty much changed; thus, the images with view zenith angle larger than 50° are not used in this study.

TABLE XI
GEOGRAPHICAL COORDINATES OF THE 20 SPOTS WHERE THE DESERT SPECTRA ARE MEASURED

Spot #	Latitude	Longitude	Spot #	Latitude	Longitude
1	39° 48′ 11.23″	102° 25′ 49.56″	11	39° 48′ 10.11″	102° 25′ 55.85″
2	39° 48′ 11.23″	102° 25′ 49.89″	12	39° 48′ 09.91″	102° 25′ 56.20″
3	39° 48′ 11.23″	102° 25′ 49.56″	13	39° 48′ 09.34″	102° 25′ 56.78″
4	39° 48′ 11.23″	102° 25′ 49.89″	14	39° 48′ 09.12″	102° 25′ 58.03″
5	39° 48′ 09.08″	102° 25′ 52.20″	15	39° 48′ 09.41″	102° 25′ 58.32″
6	39° 48′ 09.08″	102° 25′ 52.20″	16	39° 48′ 08.92″	102° 25′ 59.10″
7	39° 48′ 09.08″	102° 25′ 52.20″	17	39° 48′ 08.26″	102° 25′ 59.56″
8	39° 48′ 09.07″	102° 25′ 53.37″	18	39° 48′ 09.41″	102° 25′ 52.20″
9	39° 48′ 09.13″	102° 25′ 53.72″	19	39° 48′ 05.71″	102° 26′ 02.27″
10	39° 48′ 10.11″	102° 25′ 55.65″	20	39° 36′ 26.14″	102° 29′ 10.76″

TABLE XII
SPECTRAL MATCHING FACTOR BETWEEN HJ-1/CCD AND LANDSAT-7 ETM+

sensor / band	Spectral matching factor			
	HJA-CCD1	HJA-CCD2	HJB-CCD1	HJB-CCD2
Band1	1.048193	1.012048	1.072289	1.060241
Band2	1.017094	1.017094	1.017094	1.042735
Band3	1.011561	1.00578	0.982659	1.00578
Band4	0.992754	0.985507	0.98913	0.98913

TABLE XIII
AOD OF HJ-1/CCD IMAGES (550 nm)

Sensor	Acquisition Time (yyyy.mm.dd)	AOD (550nm)	Sensor	Acquisition Time (yyyy.mm.dd)	AOD (550nm)
HJ-1A/CCD1	20090628	0.1155	HJ-1B/CCD1	20090812	0.2146
	20090914	0.1156		20090607	0.1234
	20090814	0.2200		20090920	0.1385
	20090918	0.1161		20091025	0.1292
	20091027	0.1510		20091029	0.1653
	20090922	0.1931	HJ-1B/CCD2	20091016	0.1153
HJ-1A/CCD2	20091018	0.1162		20090602	0.2399
	20091022	0.1424		20090606	0.2221
	20090713	0.2131		20090711	0.1990
	20091026	0.2178		20091024	0.1292
	20090620	0.1970		20090614	0.1627
	20090829	0.1155		20090715	0.3694
				20090819	0.1199
				20091028	0.1851
				20091001	0.1802
				20090727	0.1888

Therefore, the BRDF and AOD derivations for higher view zenith angles are much more accurate.

4) We use the Staylor–Suttles BRDF model [21] instead of Walthall BRDF model [22] for better describing the directional characterization of the desert calibration site.

The derived AODs for all HJ-1/CCD images are listed in Table XIII.

3) HJ-1/CCD TOA Radiance Simulation and HJ-1/CCD Calibration Coefficients Calculation: With the derived HJ-1/CCD surface reflectance and AOD, the TOA radiance of HJ-1/CCD can be calculated using a radiative transfer code like 6S [15]. An example of the simulated TOA radiance and its corresponding digital number (DN) images for HJ-1A/CCD1 image on June 28, 2009, are shown in Fig. 14. The mean TOA radiance for every HJ-1/CCD image is listed in Table XIV.

From the statistics in Table XIV, the calibration coefficients for HJ-1/CCD can be calculated using

$$L = \frac{\mathrm{DN}}{A} + L_0 \tag{8}$$

where L is the TOA radiance, A is the gain, and L_0 is the offset. The unit for L and L_0 is $\mathrm{W} \cdot \mathrm{m}^{-2} \cdot \mathrm{sr}^{-1} \cdot \mu\mathrm{m}^{-1}$.

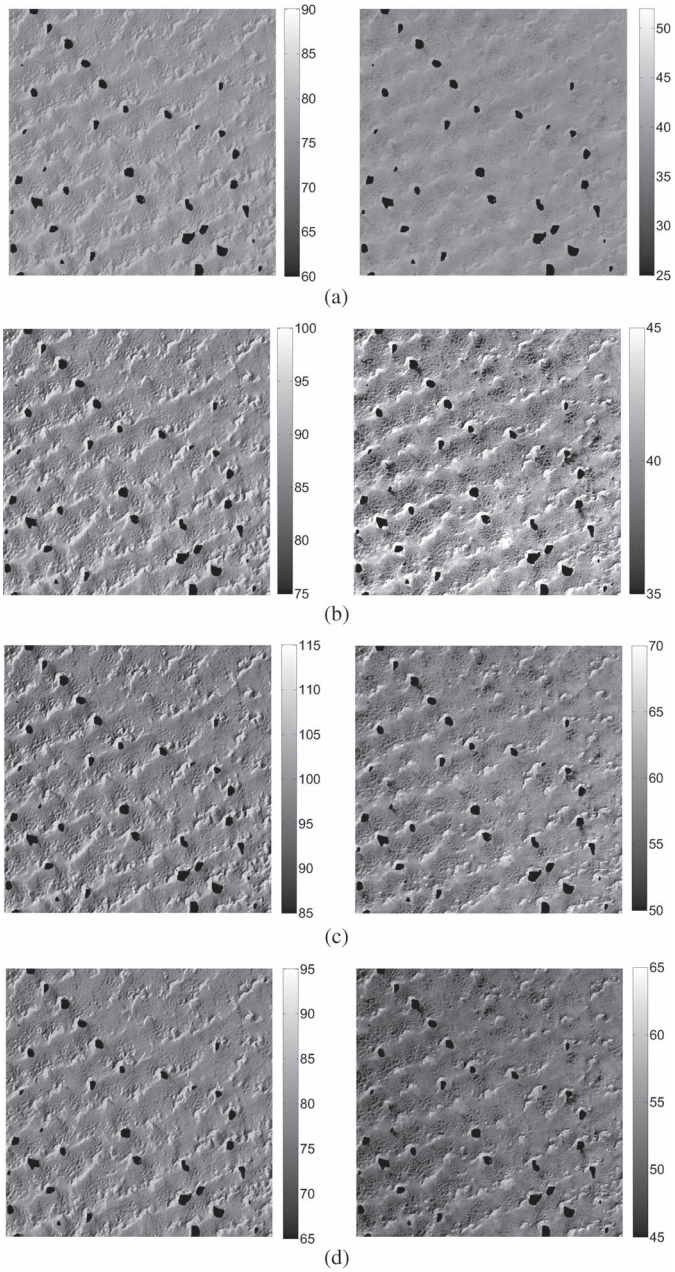

Fig. 14. Example of simulated TOA radiance and its corresponding DN of HJ-1A/CCD1 image on June 28, 2009. (a). Simulated TOA radiance and data number of Band1. (b). Simulated TOA radiance and data number of Band2. (c). Simulated TOA radiance and data number of Band3. (d). Simulated TOA radiance and data number of Band4.

TABLE XIV
MEAN OF SIMULATED TOA RADIANCES (L) AND IMAGE DN FOR HJ-1/CCD IMAGES

Band / Date	Band1		Band2		Band3		Band4	
	L	DN	L	DN	L	DN	L	DN
HJ-1A/CCD1								
20090628	79.4681	38.4951	89.0812	40.5045	99.2515	59.0769	77.6259	51.7122
20090914	70.7034	31.4745	79.2041	34.3152	86.5371	48.6626	67.4789	42.8190
20090814	71.8696	34.6702	78.7511	37.9608	86.8131	55.9110	67.8466	48.2953
20090918	62.4023	31.5234	67.8939	33.0072	75.3898	47.5512	58.9339	41.3083
20091027	51.8211	45.9572	52.1681	50.6729	55.4472	73.1179	42.684	57.5303
20090922	64.0987	30.3888	68.673	32.9803	75.4143	47.3732	58.856	42.4054
HJ-1A/CCD2								
20091018	66.7748	31.8329	69.2528	29.5739	71.6335	46.7991	55.0864	45.0109
20091022	63.3102	52.7159	65.2374	53.7512	67.0234	79.1118	51.3906	61.5115
20090713	86.3920	43.7065	94.6055	43.7716	101.6944	69.5168	77.6938	61.1719
20091026	61.0068	53.2415	62.1962	53.7085	63.1737	78.1312	47.9522	63.0612
20090620	82.2295	41.3900	91.3282	42.2521	99.4448	68.0019	76.6305	61.1131
20090829	70.3147	37.8427	78.6873	37.9039	86.7448	59.1762	67.0619	54.0457
HJ-1B/CCD1								
20090812	72.1972	36.8233	78.9327	40.8124	85.9784	59.0508	67.6947	50.7771
20090607	79.2488	37.9011	90.9000	43.0841	100.3593	63.0568	80.0387	55.1865
20090920	69.7519	32.6335	77.5246	36.1547	82.9326	51.9755	65.6245	46.4398
20091025	57.4788	47.7943	61.2876	50.6803	64.2540	75.5042	50.2290	56.7790
20091029	63.2615	47.8663	75.6649	48.4339	84.8218	72.2217	68.0045	54.2095
HJ-1B/CCD2								
20091016	68.7512	32.4233	70.5317	29.2956	72.3429	42.8823	55.2762	32.1567
20090602	95.0435	46.3423	103.2179	44.0936	109.8708	65.8182	84.1512	49.4658
20090711	89.4339	45.3688	96.6688	42.6278	103.0567	62.9534	78.4587	47.3316
20091024	61.3838	51.0582	62.7041	49.6250	63.9277	74.6216	48.3754	51.2790
20090614	85.2078	44.6942	93.0680	43.1486	99.3631	63.4271	75.8359	49.6745
20090715	92.0176	50.0155	96.7859	45.8467	100.497	65.8806	75.9533	48.6537
20090819	77.1084	39.0549	83.6056	37.4035	89.7127	55.013	68.4629	42.3466
20091028	58.4492	50.1935	59.6233	48.4833	61.5561	71.3706	46.5645	50.6672
20091001	67.2678	31.5994	71.6886	28.9635	74.6916	43.6399	56.4068	34.7217
20090727	79.8080	39.2247	88.2321	37.9921	95.5644	57.3329	73.404	44.5125

In this paper, the offset L_0 is fixed, and the prelaunch offset for each band is used; therefore, every scene of HJ-1/CCD image will produce a new gain. The average of gains from all images is used as the final gain, which is used in the validation section as follows. The results are shown in Table XV.

III. VALIDATION

A. Ground Campaign Introduction

In order to validate the cross-calibration method, the HJ-1 synchronized ground measurements of land surface spectra and atmospheric parameters at Dunhuang test site are used. The ground campaigns for HJ-1/CCD vicarious calibration have been carried out by China Center for Resources Satellite Data and Application every year since 2009. Dunhuang test site, Gansu Province, China, which is one of the China Radiometric Calibration Sites for the vicarious calibration of Chinese spaceborne sensors, was selected in 2008 by the Working Group on Calibration and Validation of the Committee on Earth Observation Satellites as one of the instrumented reference sites. The site is spatially uniform with a coefficient of variation (standard deviation/mean) less than 2% of the spectral reflectance over the 10 km by 10 km central region [23]. The details for the ground campaigns are listed in Table XVI.

B. Procedure for Validation

Using the HJ-1 synchronized ground measurements, the procedure for validation of cross-calibrating method is illustrated in Fig. 15. The procedure includes four parts.

1) Calculate the TOA radiance of Dunhuang test site using ground spectra and atmospheric parameters from ground campaigns.
2) Choose HJ-1/CCD images at Dunhuang test site synchronized with ground campaigns, and the chosen images are listed in Table XVI; calculate the TOA radiance of

TABLE XV
CALIBRATION COEFFICIENTS FOR HJ-1/CCDS USING THE NEW CROSS-CALIBRATION APPROACH

Band / Date	Band1		Band2		Band3		Band4	
HJ1A-CCD1	A	L_0	A	L_0	A	L_0	A	L_0
20090628	0.5488	9.3183	0.5069	9.1758	0.6439	7.5072	0.7038	4.1484
20090914	0.5127	9.3183	0.4900	9.1758	0.6157	7.5072	0.6761	4.1484
20090814	0.5543	9.3183	0.5456	9.1758	0.7050	7.5072	0.7582	4.1484
20090918	0.5938	9.3183	0.5621	9.1758	0.7005	7.5072	0.7540	4.1484
20090922	0.5547	9.3183	0.5543	9.1758	0.6976	7.5072	0.7751	4.1484
Mean	0.5529	9.3183	0.5318	9.1758	0.6726	7.5072	0.7334	4.1484
HJ1A-CCD2	A	L_0	A	L_0	A	L_0	A	L_0
20091018	0.5376	7.7757	0.4758	7.0944	0.6933	4.132	0.8357	1.2232
20090713	0.5544	7.7757	0.5002	7.0944	0.7125	4.132	0.7999	1.2232
20090620	0.5543	7.7757	0.5016	7.0944	0.7135	4.132	0.8104	1.2232
20090829	0.6030	7.7757	0.5294	7.0944	0.7163	4.132	0.8209	1.2232
Mean	0.5623	7.7757	0.5018	7.0944	0.7089	4.132	0.8167	1.2232
HJ1B-CCD1	A	L_0	A	L_0	A	L_0	A	L_0
20090812	0.5217	1.6146	0.5613	6.2193	0.7404	6.2193	0.7828	2.8302
20090607	0.4882	1.6146	0.5088	6.2193	0.6698	6.2193	0.7148	2.8302
20090920	0.4789	1.6146	0.5070	6.2193	0.6775	6.2193	0.7396	2.8302
Mean	0.4963	1.6146	0.5257	6.2193	0.6959	6.2193	0.7457	2.8302
HJ1B-CCD2	A	L_0	A	L_0	A	L_0	A	L_0
20091016	0.4966	3.4608	0.4531	5.8769	0.6665	8.0069	0.6928	8.8583
20090602	0.5060	3.4608	0.4530	5.8769	0.6461	8.0069	0.6570	8.8583
20090711	0.5277	3.4608	0.4695	5.8769	0.6623	8.0069	0.6800	8.8583
20090614	0.5467	3.4608	0.4949	5.8769	0.6943	8.0069	0.7417	8.8583
20090715	0.5648	3.4608	0.5043	5.8769	0.7123	8.0069	0.7251	8.8583
20090819	0.5303	3.4608	0.4812	5.8769	0.6733	8.0069	0.7105	8.8583
20090727	0.5138	3.4608	0.4613	5.8769	0.6548	8.0069	0.6896	8.8583
Mean	0.5226	3.4608	0.4697	5.8769	0.6705	8.0069	0.7034	8.8583

TABLE XVI
DETAILS OF SYNCHRONIZED GROUND CAMPAIGNS AT DUNHUANG CALIBRATION SITE AND CORRESPONDING HJ-1 IMAGERY LIST AT DUNHUANG TEST SITE AND BADAIN JARAN CALIBRATION SITE FOR CROSS-CALIBRATION VALIDATION

Ground Campaigns at Dunhuang test site			Corresponding HJ-1 data at Badain Jaran calibration site	
Campaign Date (YYYYMMDD)	Synchronous satellite and sensor	Data collected*	satellite and sensor	Date
20100812	HJ-1A/CCD2	Ground spectra and atmosphere parameters	HJ-1A/CCD2	20100818
20100816	HJ-1A/CCD1		HJ-1A/CCD1	20100811
20110914	HJ-1B/CCD2		HJ-1B/CCD2	20110928
20090825	HJ-1B/CCD1		HJ-1B/CCD1	20090920

*Ground spectra were retrieved using ASD and atmosphere parameters were retrieved by CE318. The detailed information for ASD and CE318 can be retrieved through

http://www.asdi.com/products/fieldspec-spectroradiometers/fieldspec-4-standard-res and

http://pages.usherbrooke.ca/cimel/index.php/CIMEL_318_-_general_specifications respectively.

Dunhuang test site from synchronized HJ-1/CCD images using given calibration coefficients, and the results are listed in Table XVII.

3) Choose HJ-1/CCD images at Badain Jaran desert whose date is close to that of HJ-1/CCD images of Dunhuang test site, which are listed in Table XVI; calculate the cross-calibration coefficients using the method described at the former section, and the coefficients are listed in Table XVII. Calculate the TOA radiance of Dunhuang test site using the new cross-calibration coefficients, and the results are listed in Table XVII.
4) Compare the three sets of TOA radiance of Dunhuang test site, and the comparison results are listed in Table XVII.

C. Comparisons and Analyses

In this validation, four ground campaigns synchronized with all four CCDs (1A/CCD1, 1A/CCD2, 1B/CCD1, and 1B/CCD2) have been done in three consecutive years from 2009 to 2011. The details of the campaigns are listed in Table XVI. The validation results are listed in Table XVII. By comparisons of the TOA radiance from ground measurements, cross-calibration coefficients, and given calibration coefficients, it shows the following.

1) Compared to TOA radiance from ground measurements, all errors of the TOA radiance from the new cross-calibration method are less than 5% or close to 5%.

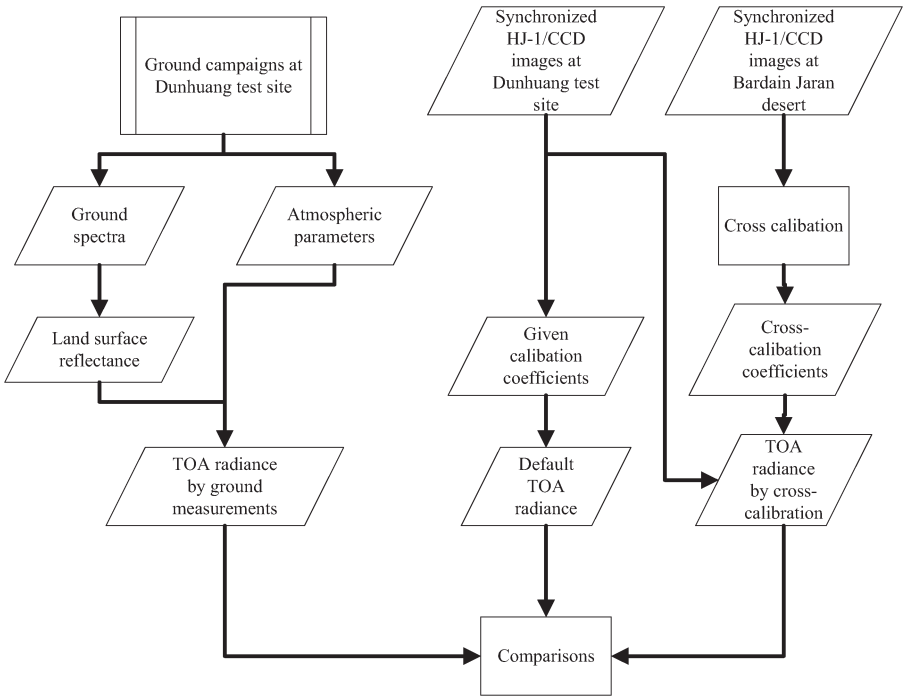

Fig. 15. Cross-calibrating validation procedure through comparison of TOA radiances by calculating using ground measurements, given calibration coefficients, and cross-calibration coefficients, respectively.

TABLE XVII
HJ-1/CCD CROSS-CALIBRATION VALIDATION RESULTS

Date(YY MMDD)	Satellite/ sensor	band	Offset	CCC*	GCC$	TOA radiance by CCC	TOA radiance by GCC	TOA radiance by GM#	Error by CCC	Error by GCC
100811	1A/CCD1	Band1	7.3250	0.8100	0.6925	114.3622	132.5310	108.7449	0.0516	0.2187
		Band2	6.0737	0.8155	0.7438	111.3873	121.5427	110.5042	0.0079	0.0998
		Band3	3.6123	1.0807	0.9636	97.2444	108.6270	101.1343	0.0384	0.0740
		Band4	1.9028	1.0544	1.0545	67.0518	67.04755	70.85944	0.0537	0.0537
110928	1B/CCD2	Band1	2.2219	0.8492	0.8352	96.4577	98.03807	96.3980	0.0006	0.0170
		Band2	4.0683	0.8761	0.7925	92.1127	101.4051	93.1440	0.0110	0.0887
		Band3	5.2537	1.1585	1.1316	87.7656	89.7307	85.3340	0.0284	0.0515
		Band4	6.3497	1.0941	1.0578	60.8876	62.7592	59.2300	0.0279	0.0596
100812	1A/CCD2	Band1	4.6344	0.9794	0.9230	107.1702	113.4408	110.8736	0.0334	0.0231
		Band2	4.0982	0.9016	0.9399	108.1073	103.8745	107.0163	0.0101	0.0293
		Band3	3.7360	1.2163	1.3093	100.9593	94.0571	96.05768	0.0510	0.0208
		Band4	1.3178	1.2564	0.7385	68.3588	115.3811	66.1060	0.0340	0.7453
09025	1B/CCD1	Band1	1.6146	0.4963	0.4817	103.4974	106.5854	105.879	0.0230	0.0066
		Band2	6.2193	0.5257	0.4728	102.2621	113.008	105.094	0.0276	0.0753
		Band3	6.2193	0.6959	0.6262	96.0534	106.0525	97.1140	0.0110	0.0920
		Band4	2.8302	0.7457	0.7007	68.5089	72.7268	66.4500	0.0300	0.0944

*CCC is abbreviation of Cross-Calibration Coefficients.
$GCC is abbreviation of Given Calibration Coefficients.
#GM is abbreviation of Ground Measurements.

2) Compared to TOA radiance from ground measurements, most of the errors of the TOA radiance from the given calibration coefficients are larger than 5%.

3) Almost all errors of TOA radiance from the cross-calibration method are less than that from the given calibration coefficients.

Therefore, the proposed cross-calibration method performs very well for different HJ-1/CCD cameras in consecutive years and satisfies the requirement of 5% error from ground measurements for radiometric calibration procedure. Compared to the given calibration coefficients provided once every year, the cross-calibration method can provide the calibration coefficients as much as possible only if there is HJ-1/CCD imagery at the Badain Jaran desert calibration site without cloud contamination; the cross-calibration method proposed in this paper, thus, can be made a routine procedure for cross-calibrating HJ-1/CCDs.

IV. Conclusion and Discussion

In this paper, a new cross-calibration method for HJ-1/CCDs has been proposed by using Landsat ETM+ imagery. Although the wide swath coverage of HJ-1/CCD made a much shorter revisiting period than Landsat ETM+, the much larger view angles close to 50° made them difficult to be cross-calibrated using similar sensors like Landsat TM/ETM+, which are mostly observing the Earth in nadir. The Badain Jaran desert calibration site has a homogeneous surface material, which is sand, but the topography is hilly. This affords a wide range of local slopes and aspects of the same basic material, a natural data set for characterizing the material BRDF. Based on the aforementioned fact, the well-calibrated Landsat ETM+ imagery and ASTER GDEM product are used together to retrieve the BRDF characterization of Badain Jaran desert calibration site and cross-calibrate HJ-1/CCDs. Based on the validation using data from ground campaigns at Dunhuang test site, the new method performs very well for different HJ-1/CCD sensors in consecutive years and satisfies the requirement of 5% error from ground measurements for radiometric calibration procedure. Compared to the given calibration coefficients provided once every year, the cross-calibration method can provide the calibration coefficients as much as possible only if there is HJ-1/CCD imagery at Badain Jaran desert calibration site without cloud and haze contamination; the cross-calibration method proposed in this paper, thus, can be proposed as a routine procedure for cross-calibrating HJ-1/CCDs.

The horizontal resolution of ASTER GDEM product used in this method is only a litter higher than 120 m, and the accuracy is highly correlated to the resolution of DEM; therefore, this method can be improved with the use of ASTER GDEM product version 2 or even higher resolution DEM product.

Acknowledgment

The HJ-1/CCD remote sensing data and ground measurements at Dunhuang test site used in this research are supported by the China Centre for Resources Satellite Data and Application (http://www.cresda.com). The Landsat TM/ETM+ data were downloaded from the U.S. Geological Survey Web site (http://landsat.usgs.gov). The ASTER global digital elevation model data were downloaded from Japan Space System (http://gdem.ersdac.jspacesystems.or.jp). The MODIS data were downloaded from the Level 1 and Atmosphere Archive and Distribution System (http://laadsweb.nascom.nasa.gov).

References

[1] K. J. Thome, B. Markham, J. Barker, P. N. Slater, and S. F. Biggar, "Radiometric calibration of Landsat," *Photogramm. Eng. Remote Sens.*, vol. 63, no. 7, pp. 853–858, Jul. 1997.

[2] J. E. Vogelmann, S. M. Howard, L. Yang, C. R. Larson, B. K. Wylie, and J. N. VanDriel, "Completion of the 1990's national land cover data set for the conterminous United States," *Photogramm. Eng. Remote Sens.*, vol. 61, pp. 299–305, Jun. 2001.

[3] B. L. Markham, K. Thome, J. Barsi, E. Kaita, D. Helder, J. Barker, and P. Scaramuzza, "Landsat-7 ETM+ On-orbit reflective-band radiometric stability and absolute calibration," *IEEE Trans. Geosci. Remote Sens.*, vol. 42, no. 12, pp. 2810–2820, Dec. 2004.

[4] P. M. Teillet, J. L. Barker, B. L. Markham, R. R. Irish, G. Fedosejeves, and J. C. Storey, "Radiometric cross-calibration of the Landsat-7 ETM+ and Landsat-5 TM sensors based on tandem data sets," *Remote Sens. Environ.*, vol. 78, no. 1/2, pp. 39–54, Oct. 2001.

[5] G. Chander and B. L. Markham, "Revised Landsat-5 TM radiometric calibration procedures and post-calibration dynamic ranges," *IEEE Trans. Geoscie. Remote Sens.*, vol. 41, no. 11, pp. 2674–2677, Nov. 2003.

[6] D. L. Helder and T. A. Ruggles, "Landsat Thematic Mapper reflective band radiometric artifacts," *IEEE Trans. Geosci. Remote Sens.*, vol. 42, no. 12, pp. 2704–2716, Dec. 2004.

[7] P. M. Teillet, D. L. Helder, T. A. Ruggles, R. Landry, F. J. Ahern, N. J. Higgs, J. Barsi, G. Chander, B. L. Markham, J. L. Barker, K. J. Thome, J. T. Schott, and F. D. Palluconi, "A definitive calibration record for the Landsat-5 Thematic Mapper anchored to the Landsat-7 radiometric scale," *Can. J. Remote Sens.*, vol. 30, no. 4, pp. 631–643, Aug. 2004.

[8] G. Chander, D. J. Meyer, and L. Dennis, "Cross calibration of the Landsat-7 ETM+ and EO-1 ALI sensor," *IEEE Trans. Geosci. Remote Sens.*, vol. 42, no. 12, pp. 2821–2831, Dec. 2004.

[9] P. Henry, M. Dinguirard, and M. Bidilis, "SPOT multitemporal calibration over stable desert areas," in *Proc. SPIE Int. Symp. Aerosp. Remote Sens.*, Orlando, FL, USA, Apr. 12–16, 1993, pp. 67–76.

[10] F. Cabot, O. Hagolle, H. Cosnefroy, and X. Briottet, "Intercalibration using desertic sites as a reference target," in *Proc. Geosci. Remote Sens. Symp.*, Seattle, WA, USA, Jul. 6–10, 1998, vol. 5, pp. 2713–2715.

[11] H. Cosnefroy, M. Leroy, and X. Briottet, "Selection and characterization of Saharian and Arabian desert sites for the calibration of optical satellite sensors," *Remote Sens. Environ.*, vol. 58, no. 1, pp. 101–114, Oct. 1996.

[12] D. Helder, B. Basnet, and D. Morstad, "Optimized identification of worldwide radiometric pseudo-invariant calibration sites," *Can. J. Remote Sens.*, vol. 36, no. 5, pp. 527–539, Oct. 2010.

[13] S. Lachérade, B. Fougnie, P. Henry, and P. Gamet, "Cross calibration over desert sites: Description, methodology, operational implementation," *IEEE Trans. Geosci. Remote Sens.*, vol. 51, no. 3, pp. 1098–1113, Mar. 2013.

[14] P. S. Chavez, Jr., "Image-based atmospheric corrections—Revisited and revised," *Photogramm. Eng. Remote Sens.*, vol. 62, no. 9, pp. 1025–1036, Sep. 1996.

[15] E. F. Vermote, D. Tanre, J. L. Deuze, M. Herman, and J. J. Morcette, "Second simulation of the satellite signal in the solar spectrum 6S: An overview," *IEEE Trans. Geosci. Remote Sens.*, vol. 35, no. 3, pp. 675–686, May 1997.

[16] J. D. Wood, "The Geomorphological Characterisation of Digital Elevation Models," Ph.D. dissertation, Univ. Leicester, Leicester, U.K., 1996.

[17] J. Dozier and J. Frew, "Rapid calculation of terrain parameters for radiation modeling from digital elevation data," *IEEE Trans. Geosci. Remote Sens.*, vol. 28, no. 5, pp. 963–969, Sep. 1990.

[18] J. Sun, A. Angal, X. Xiong, H. Chen, X. Geng, A. Wu, T. Choi, and M. Chu, "MODIS RSB calibration improvements in Collection 6," in *Proc. SPIE*, Oct. 2012, vol. 8528.

[19] S. Liang, B. Zhong, and H. Fang, "Improved estimation of aerosol optical depth from MODIS imagery over land surfaces," *Remote Sens. Environ.*, vol. 104, no. 4, pp. 416–425, May 2006.

[20] B. Zhong, S. Liang, and B. Holben, "Validating a new algorithm for estimating aerosol optical depths over land from MODIS imagery," *Int. J. Remote Sens.*, vol. 28, no. 18, pp. 4207–4214, Sep. 2007.

[21] W. D. Staylor and J. T. Suttles, "Reflection and emission models for desert derived from Nimbus-7 ERB scanner measurements," *Climate Appl. Meteorol.*, vol. 25, pp. 196–202, 1986.

[22] C. L. Walthall, J. M. Norman, G. Campbell, and B. L. Blad, "Simple equation to approximate the bi-directional reflectance from vegetation canopies and bare soil surfaces," *Appl. Opt.*, vol. 24, pp. 675–686, Feb. 1985.

[23] C. Hu, F. E. Muller-Karger, S. Andrefouet, and K. L. Carder, "Atmospheric correction and cross-calibration of LANDSAT-7/ETM+ imagery over aquatic environments: A multiplatform approach using Seawifs/MODIS," *Remote Sens. Environ.*, vol. 78, pp. 99–107, Nov. 2001.

Bo Zhong received the M.S. degree from the Institute of Remote Sensing Applications, Chinese Academy of Sciences, Beijing, China, in 2004 and the M.A. degree from the University of Maryland, College Park, MD, USA, in 2006.

He is currently an Assistant Research Scientist with the State Key Laboratory of Remote Sensing Science, jointly sponsored by the Institute of Remote Sensing and Digital Earth, Chinese Academy of Sciences, and Beijing Normal University, Beijing. His research interests include land-use and land-cover changes, remote sensing image processing, and remote sensing of aerosol.

Yuhuan Zhang received the M.S.degree in photogrammetry from Shandong University of Science and Technology, Qingdao, China. She is currently working toward the Ph.D. degree in cartography and geography information system in the Institute of Remote Sensing and Digital Earth, Chinese Academy of Sciences, Beijing, China.

Her scientific interests include in-flight calibration for remote sensing satellite sensors, atmospheric remote sensing, and atmospheric correction.

Tengteng Du received the M.E. degree from Shandong University of Science and Technology, Qingdao, China, in 2013.

He is currently with Space Star Technology Company, Ltd., Beijing, China. His study interests include atmospheric correction and remote sensing image processing.

Aixia Yang received the B.S. degree from Chongqing University of Posts and Telecommunications, Chongqing, China, in 2011, where she is currently working toward the M.E. degree in the College of Computer Science and Technology.

Her study interests includes cross-calibration and validation.

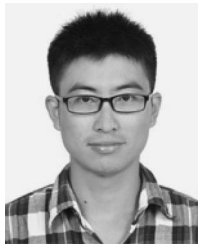

Wenbo Lv received the B.E. degree from Southwest Petroleum University, Chengdu, China, in 2011. He is currently working toward the M.E. degree in the College of Geosciences and Environmental Engineering, Southwest Jiaotong University, Chengdu.

His study interests are cross-calibration of optical sensors and pseudoinvariant feature extraction.

Qinhuo Liu received the B.Sc. degree in hydrogeology and engineering geology from Southwest Jiaotong University, Chengdu, China, in 1988 and the M.Sc. degree in cartography and remote sensing and the Ph.D. degree in atmospheric physics from Peking University, Beijing, China, in 1994 and 1997, respectively.

He was with the Institut National de la Recherche Agronomique, Paris, France, in 1998, Boston University, Boston, MA, USA, in 1999, University of Maryland, College Park, MD, USA, in 2004, and George Mason University, Fairfax, VA, USA, in 2010 as short-term Visiting Scholar. From 1997 to 2012, he was with the Institute of Remote Sensing Applications, Chinese Academy of Sciences (CAS), Beijing. He is currently a Professor and the Deputy Director of the State Key Laboratory of Remote Sensing Science, Institute of Remote Sensing and Digital Earth, CAS. His research interests focus on radiation transfer modeling for optical remote sensing, terrestrial parameter inversion from multisource remote sensing data, and quantitative remote sensing applications for land surface energy balance.

Prof. Liu is a member of the IEEE Geoscience and Remote Sensing Society.